

# Multifractal topography of several planetary bodies in the Solar System

François Landais<sup>\*,a</sup>, Frédéric Schmidt<sup>a</sup>, Shaun Lovejoy<sup>b</sup>

<sup>a</sup> GEOPS, Univ. Paris-Sud, CNRS, Université Paris-Saclay, Rue du Belvédère, Bât. 504-509, Orsay 91405, France

<sup>b</sup> Physics, McGill University, 3600 University St, Montreal, QC H3A2T8 Canada



## ARTICLE INFO

### Keywords:

Topography  
Comparative planetology  
Surface  
Fractal  
Scaling  
Multifractal

## ABSTRACT

Topography is the expression of both internal and external processes of a planetary body. Thus hypsometry (the study of topography) is a way to decipher the dynamics of a planet. For that purpose, the statistics of height and slopes may be described by different tools, at local and global scale. We propose here to use the *multifractal* approach to describe fields of topography. This theory encompasses height and slopes and other statistical moments of the field, taking into account the scale invariance. Contrary to the widely used *fractal* formalism, *multifractals* are able to describe the intermittency of the topography field. As we commonly observe a juxtaposition of rough and smooth topographies at a given scale, the *multifractal* framework seems to be appropriate for hypsometric studies. Here we analyze the data at global scale of the Earth, Mars, Mercury and the Moon and find that the statistics are in good agreement with the *multifractal* theory for scale larger than  $\sim 10$  km. Surprisingly, the analysis shows that all bodies have the same *fractal* behavior for scale smaller than  $\sim 10$  km. We hypothesize that dynamic topography of the mantle may be the explanation at large scale, whereas the smaller scale behavior may be related to elastic thickness.

## 1. Introduction

The scaling of coastlines was empirically studied by Richardson (1961) and Mandelbrot (1967) interpreted his results in terms of fractals. Fractals are geometric sets of points that have a scale symmetry. Geophysical examples of scaling include turbulent phenomena including clouds, the wind, the ocean, river flows, as well as various solid earth fields including rock faults and topography. Most systems of geophysical interest are mathematical fields, not geometric sets. When scaling, they will generally be multifractals. A general way to quantify this is to determine the statistical moments of fluctuations of the field, (generalized) structure functions. Denoting the fluctuation in the topography over a distance  $\Delta x$  by  $\Delta h(\Delta x)$ , the  $q$ th order structure function is  $(\Delta h(\Delta x))^q$ . If the system is scaling, then this is a power law of the lag  $\Delta x$ :  $\Delta x^{\zeta(q)}$ . The field is *monofractal* if  $\zeta(q) = qH$  where  $H$  is named in honor of Hurst; in this linear case the field is quasi-Gaussian. In the more general multifractal case,  $\zeta(q) = qH - K(q)$  where  $K(q)$  is a convex function with  $K(1) = 0$ , it determines the multifractality, the intermittency, the “spikiness” of the field. Numerous studies have shown that in several contexts, topography is scaling over a significant range of scales (see the review of Dodds and Rothman, 2000).

For multifractal processes, local estimates of fractal dimensions will be different from one location to another, they will be stochastic. It is

thus possible to interpret the topography of regions with quite different slope distributions in a unified multifractal framework. This suggests that even a global analysis of the topography of a planet might be scaling and multifractal despite of its diversity and complexity. Previous studies have established that the Earth’s topography is to a good approximation multifractal over a very wide range of scales (Lavalée et al., 1993; Gagnon et al., 2006). In the general case,  $\zeta(q)$  is a concave function; in order to characterize or model multifractals one takes advantage of the existence of stable, attractive statistical behavior: universality classes (Schertzer and Lovejoy, 1987).

In a previous analysis, we performed a global analysis on the topographic MOLA data from Mars (Smith, 2001). We also found a good agreement with universal multifractals but we found two scaling ranges with different characteristics (Landais et al., 2015). The statistical structure was found to be different at small scales (nearly monofractal) and large scales (multifractal) with a transition occurring at around 10 km. This behavior has been confirmed recently with other analyses (Deliege et al., 2016).

The goal of this article is to extend this pioneering Martian work to all planetary bodies whose topography is well estimated: the Earth, the Moon and Mercury. There is topography data for Venus and Titan but unfortunately too much data is missing to allow for a similar analysis on the global scale.

\* Corresponding author.

E-mail address: [francois.landais@u-psud.fr](mailto:francois.landais@u-psud.fr) (F. Landais).

<https://doi.org/10.1016/j.icarus.2018.07.005>

Received 11 May 2017; Received in revised form 2 July 2018; Accepted 6 July 2018

Available online 29 August 2018

0019-1035/ © 2018 Elsevier Inc. All rights reserved.

**Table 1**  
Characteristics of the datasets.

	Source	Radius (km)	Resolution	min scale	max scale	Lines	Columns	no. fluctuations
Earth	ETOPO1	6371	60 px/deg	1 853 m	20,015 km	10,800	21,600	0.2 billions
Mars	MOLA	3390	128 px/deg	462 m	10,650 km	22,528	46,080	1 billion
Moon	LOLA	1737	512 px/deg	60 m	5457 km	92,160	184,320	13 billions
Mercury	MLA	2240	64 px/deg	665 m	7037 km	11,520	23,040	0.0002 billion

## 2. Universal multifractal theory

We first define the fluctuations  $\Delta h(\Delta x)$ . The simplest definition is the altitude differences, the slopes multiplied by  $\Delta x$ , the most natural indicator of roughness. But there are many other ways to define fluctuations. Wavelets provide a general method. Indeed, their coefficients define fluctuations (with appropriate normalization). The simple altitude difference corresponds to the “poor man” wavelet and can be advantageously replaced by the Haar wavelet that is more accurate and is useful over a wider range of exponents ( $-1 < H < 1$  rather than  $0 < H < 1$  for differences), see [Lovejoy \(2014\)](#) and paragraph below for a precise definition of Haar fluctuations.

*Statistical moments.* We can compute any statistical moment  $M_q$  of order  $q$  defined by:

$$M_q(\Delta x) = \langle \Delta h(\Delta x)^q \rangle \quad (1)$$

with  $\langle \rangle$ , denoting the statistical average. If  $q = 2$ , it simply correspond to the variance. In principle, every order (even non-integer orders) must be computed to fully reveal the whole variability of the data. If the field is scaling, all the statistical moments are expected to follow a power-law with scale.

*Multifractality.* Scaling allows us to introduce two distinct statistical processes: monofractal and multifractal. For a detailed description of the formalism we apply in this study, the reader can refer to [Lovejoy and Shertzer \(2013\)](#) briefly summed up in [Landais et al. \(2015\)](#). We now quickly recall the main notions.

- In the usual gaussian monofractal case the parameters  $H$  is sufficient to describe the statistic of all the moments of order  $q$  (Eq. (2)). There is no intermittency, meaning that the roughness of the field is spatially homogenous despite its fractal variability regarding scales. For example, the value  $H = 0.5$  corresponds to the classic Brownian motion. This kind of statistical object has proved to be relevant in many local and regional analysis of natural surfaces ([Orosei et al., 2003](#); [Rosenburg et al., 2011](#)), at least over restricted ranges of scales but fails to give full account to the intermittency commonly observed on larger topographic datasets.

$$M_q \sim \Delta x^{qH} \quad (2)$$

- In the multifractal case,  $H$  is not sufficient to fully describe the statistics of the moments of order  $q$ . An additional convex function  $K(q)$  depending on  $q$  is required (see Eq. (3)). The moment scaling function  $K$  modifies the scaling law of each moment. The consequence for the corresponding field appears clearly in simulations ([Gagnon et al., 2006](#)): the field exhibits a juxtaposition of rough and smooth places that are clearly more realistic in the case of natural surfaces. Moreover, it is possible to restrain the generality of the function  $K(q)$ , considering only universal multifractals, a stable and attractive class proposed by [Schertzer and Lovejoy \(1987\)](#) for which the multifractality is completely

determined by the mean intermittency  $C_1 = \left( \frac{dK(q)}{dq} \right)_{q=1}$  (codimension of the mean) and the curvature  $\alpha$  of the function  $K$ ,  $\alpha = \frac{1}{C_1} \frac{d^2K(q)}{dq^2}$  (the degree of multifractality). In that case the expression of  $K$  is simply given by Eq. (5).

$$M_q \sim \Delta x^{qH-K(q)} \quad (3)$$

$$\xi(q) = qH - K(q) \quad (4)$$

$$K(q) = \frac{C_1}{\alpha - 1} (q^\alpha - q) \quad (5)$$

We see that the monofractal case corresponds to ( $H \neq 0, C_1 = 0$ ) or ( $H \neq 0, C_1 \neq 0, \alpha \rightarrow 0$ ).

## 3. Dataset

The topography of a planet is defined as the difference between the distance of the planetary surface and the geoid. For Mars ([Smith, 2001](#)), Mercury ([Cavanaugh, 2007](#)) and the Moon ([Smith, 2010](#)), we are used topographic data stored in PDS (Planetary Data System, <http://pds-geosciences.wustl.edu>) whereas the Earth data ([Amante and Eakins, 2009](#)) are gathered from numerous global and regional data sets. Table 1 sums up the main characteristics of the datasets. Each has already been previously analyzed.

The Earth has been studied for multifractal purpose by [Gagnon et al. \(2006\)](#) using ETOPO5 dataset. They analyzed separately continents and oceans and found that  $H$  is varying from 0.46 for bathymetry and 0.66 for continent. The dataset considered in our study (ETOPO1, [Amante and Eakins, 2009](#)) is an arc-minute global relief model of the Earth.

On Mars, the main source of topographic data is the Laser altimeter MOLA ([Smith, 2001](#)) that allows to perform extensive statistical analysis with different roughness indicators on sliding windows revealing interesting correlation with geological units ([Aharonson et al., 2001](#); [Kreslavsky and Head, 2000](#)). The monofractal scaling of the topography of Mars has also been studied by [Orosei et al. \(2003\)](#) through the local computation of the scale independent Hurst parameters revealing a high disparity of values across the Martian surfaces as expected for multifractal topography.

On the Moon, the high-precision topographic data obtained by the laser altimeter LOLA ([Smith, 2010](#)) has been extensively used. [Kreslavsky et al. \(2013\)](#) computed maps of roughness at hectometer and kilometer scales revealing poor correlations between these two scales. Moreover, [Rosenburg et al. \(2011\)](#) measured  $H$ . They not only identified a transition that occurs around 1 km at most location but they also found significantly different values of  $H$  in the Highlands ( $H = 0.95$ ) and in the Maria ( $H = 0.76$ ).

On Mercury, by using the MLA data ([Cavanaugh, 2007](#); [Pommerol et al., 2012](#)) computed roughness indicators on extracted profiles from geologically distinct regions. Due to the eccentricity of the orbit, only the northern hemisphere could be mapped by laser altimetry with a resolution of about 5 km. The use of pairs of stereoscopic images has finally made it possible to develop an overall map of the topography of Mercury ([Solomon, 2001](#); [Hawkins, 2007](#)). We analyzed both MLA data

only and the full map (from both laser and stereoscopy) and found no significant difference, except for the fact that the larger scales are available for the full map. We thus choose to present here only the full map results. This result confirms that there is no significant bias (at least regarding multifractal properties) between stereoscopic and laser altimetric techniques.

The current study proposes to extend the scope of the multifractal analysis already performed on Earth and Mars (Gagnon et al., 2006; Landais et al., 2015) to all the bodies in the solar system for which data is adequate. Thus the case of the Earth, Mars, Moon and Mercury will be discussed and compared. The case of Venus is not considered here despite of the existence of a dataset collected by Magellan because of the relative lack of topographic data (Ford et al., 2014). The same is true for Titan (Stiles, 2009).

#### 4. Methodology

In our previous analysis (Landais et al., 2015), we considered the 1-D topographic profiles directly extracted from the along-track measurement of MOLA stored in PDS (<http://pds-geosciences.wustl.edu>, Smith, 2001). As the data are irregularly sampled due to the presence of clouds and instrument problems, we used multifractal simulations to study the effect of a MOLA-like irregular signal on the Haar fluctuations. It turned out that, most probably due to the small fraction of missing data, the irregularity had no detectable impact on the analysis. We also found that the use of the gridded data also produced the same results as the direct use of the more reliable along-track measurement, the conclusion being that for the purpose of a global analysis, the extrapolated gridded map for each body is sufficient to recover the global statistical parameters. The methodology used here is therefore much simpler and only relies on the gridded data. We only considered 1D North-South profiles and computed the Haar fluctuations at different lags  $\Delta x$ . The simplification to 1-D is reasonable as we perform a global statistical analysis. In addition, the North/South direction is more relevant than East–West because each profile has the same length. Fig. 1a provides an example of 1-D profiles extracted from the gridded field for each body. See Landais et al. (2015) for a review of the different biases that could result from such an approach. We also addressed the issue of finite-size effects that may have an impact on the small scales.

We implicitly consider that the global statistics are isotropic. This assumption is reasonable for the purpose of a global analysis given the fact that shape of various orientation can be found on a given body. Although local anisotropy is commonly observed (Kreslavsky and Head, 2003; Bondarenko et al., 2006; Bills et al., 2014), we assume it is erased

by the spatial averaging. Isotropic multifractal processes readily produce strong local anisotropy so that the question of systematic scale dependent statistical anisotropy is not easy to establish. Anisotropy remains an important issue and will be more carefully considered in future works.

*Haar fluctuations and statistical moments.* At a given location  $x$  and a given scale  $\Delta x$  corresponding to  $N$  successive elevation data on the grid, we average separately the first  $\frac{N}{2}$  points  $M_1(x, \Delta x)$  and last  $\frac{N}{2}$  points  $M_2(x, \Delta x)$ . The Haar fluctuation is simply defined as the difference  $S(x, \Delta x) = |M_2(x, \Delta x) - M_1(x, \Delta x)|$ . This definition is illustrated by Fig. 1b. The Mean Haar Fluctuation (MHF, moment of order 1) is simply obtained by averaging all the available Haar fluctuations in a dataset. By extension, other statistical moments of any order  $q$ ,  $MHF_q$  may be computed by averaging the fluctuations raised to the power of  $q$ :

$$MHF = \langle S(x, \Delta x) \rangle$$

$$MHF_q = \langle S(x, \Delta x)^q \rangle$$

#### 5. Results for Earth, Mars, Mercury and the Moon

*Mean Haar Fluctuations (MHF).* Fig. 2 shows the Mean Haar Fluctuations for each body on a log-log plot. One can observe its scaling behavior as a function of the real distance (in meters). One can observe that at small scale,  $MHF$  ranges from the larger to the smaller for: the Moon, Mercury, Mars, the Earth. This simply means that statistically, the roughness is from the larger to the smaller: for the Moon, Mercury, Mars, the Earth. Thus an astronaut (coming from the Earth) would experience differently the landscape of other planetary bodies. He would feel smaller in front of a rougher landscape at his/her scale. This feeling should be largest for the Moon. Another interesting feature is the resemblance between i) the curves of Earth and Mars and ii) the curves of the Moon and Mercury. For the two small bodies, the  $MHF$  is clearly above the two others, except at the largest scales. By interpreting it as a roughness indicator, this feature simply reflects the well-known high level of roughness of small bodies, a consequence of

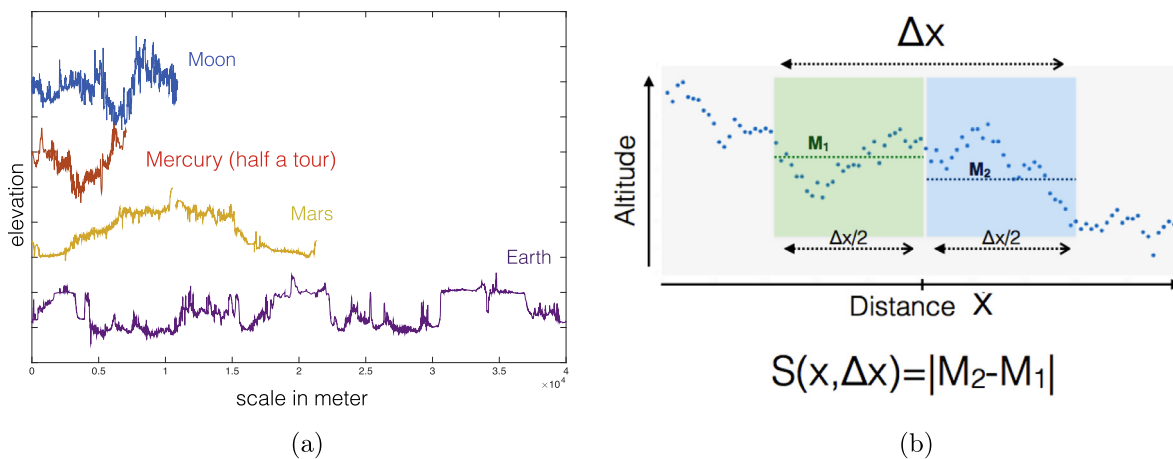


Fig. 1. (a) Topographic dataset: 4 typical profiles, 1 for each body in the scope of this study. The length corresponds to 1 complete circumference of the planets except in the case of Mercury (only half a circumference) (b) Definition of the Haar fluctuation used to perform the statistical analysis.  $M_1$  (respectively  $M_2$ ) is the average of the first half (respectively second half) of the topographic profile.

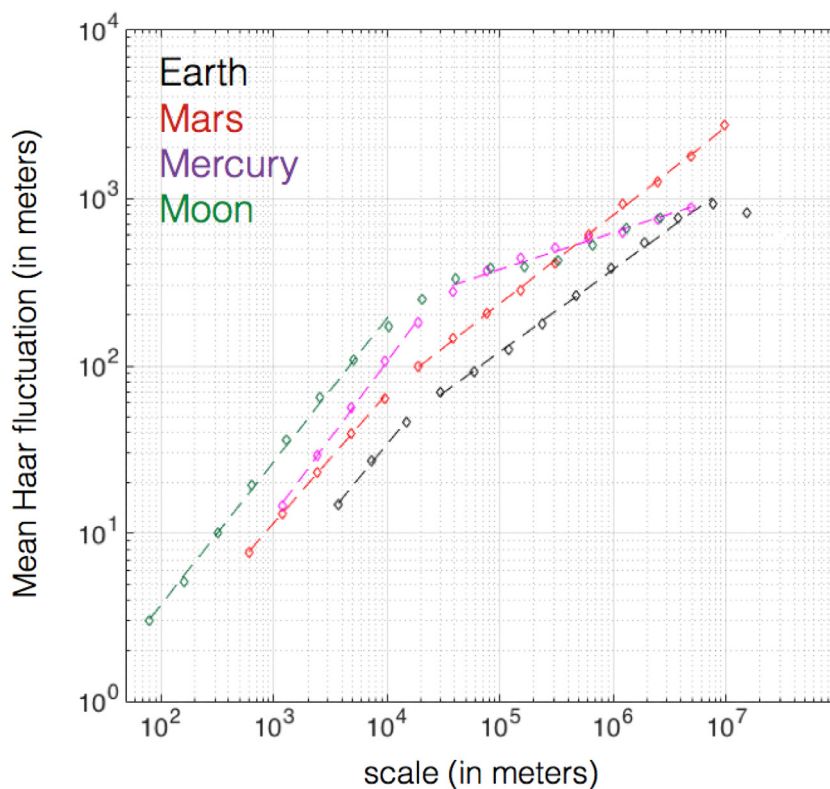


Fig. 2. Mean Haar fluctuations  $MHF$  (order 1) as a function of scales for the 4 planetary bodies.

intense cratering shaping their surfaces.

As expected, the global  $MHF$  increases with scale in all cases, simply reflecting the fact that larger scales yield larger differences in elevation. Nevertheless for the Earth and Mercury, at large scales, the  $MHF$  begins to decrease before reaching its maximum scale. More specifically, as our goal is to study the global scaling behavior of topography, we expect this global increase of the  $MHF$  to be linear on a log-log plot. It is clearly not the case over the entire available range of scales. Still noticeable scaling appears but over restricted ranges of scale: a transition seems to occur, separating two distinct scaling regimes. Such a transition is observed for all the bodies and interestingly, it occurs at around 10–20 km in each case including the Moon. The nature of this transition, discussed in our previous analysis focused on Mars and already pointed out by other authors in the case of Mars (Malamud and Turcotte, 2001), remains unknown.

In Fig. 3, the  $MHF$  are normalized by their respective values around 10 km in order to emphasize the transition at that scale. As one can see, the slope at small scales ( $< 10$  km) are rather similar ( $H \sim 0.8$ ) whereas significantly different slopes are observed at large scales ( $H \sim 0.2-0.5$ ). The scaling is excellent at large scales in the case of Mars and good in the case of Earth and Mercury. In the case of the Moon, data points are more dispersed, and  $H$  might be less well defined. Note also at small scales, the available range for Earth and Mercury is limited and might result in an unconvincing fit. The values obtained for  $H$  for each body by computing a linear regression on the distinct ranges of scale is reported on Table 2.

**Statistical moments  $MHF_q$ .** In the case of universal multifractals, all the statistical moments will scale according to Eq. (3), the  $MHF$  being the particular case for which  $q = 1$ . Thus we can estimate the other multifractal exponents by computing statistical moments  $MHF_q$ . On Fig. 4, the  $MHF_q$  are plotted for different values of  $q$  and for the different bodies. The next step is to compute linear regressions on every curve and on the distinct identified scaling regime. The log-log slopes  $\zeta(q)$  may then be plotted as a function of  $q$  for each body and for each

range of scales (see Fig. 5) in order to visualize the function  $\xi$  defined by Eq. (4). A linear  $\zeta(q)$  is the signature of monofractality whereas a curved  $\zeta(q)$  indicates a multifractal behavior according to Eqs. (2) and (3). Interestingly, Fig. 5 clearly shows that on the distinct scaling regimes (low scale and large scales) the behavior is significantly different. Over the range of small scales ( $< 10$  km, plot on the left), the curves are rather similar for all the four bodies and are very close to straight lines indicating that the statistics are found to be roughly monofractal (small  $C_1$ ) over the range. Over the range of large scales ( $> 10$  km, plot on the right), we obtained curved structure functions in most cases revealing the multifractal nature of the statistics of topography over the range. The multifractal parameters are computed according to Eq. (3) and reported on Table 2. Whereas the case of Mars, Mercury and Earth have similar values of  $C_1$  around 0.1, the case of the moon seems to be an exception with weak multifractal properties over the whole range of scales ( $C_1$  close to 0).

## 6. Discussion and conclusion

By averaging the fluctuations at different scales, we have revealed global statistical pattern of planetary bodies. We tested and validated the multifractal approach on the four bodies with empirically well estimated topography: the Earth, Mars, Mercury and the Moon. We found that a transition occurs at about 10 km and that it is a general property of all planetary topographies. Below 10 km, differences in altitudes decrease more rapidly when the scale decreases.

As suggested by Araki (2009) and Nimmo et al. (2011), for the transition in the topographic power spectral density, we propose the interpretation that the elastic thickness of the lithosphere is responsible for this transition by acting against the deformations caused by the different surface processes in two regimes. At scales smaller than the elastic thickness  $T_e$ , a modification of the surface (for example, following an impact) does not make it possible to generate isostatic compensation. The new relief can therefore remain. The slopes of neighboring facets tend to be correlated with each other and give rise to

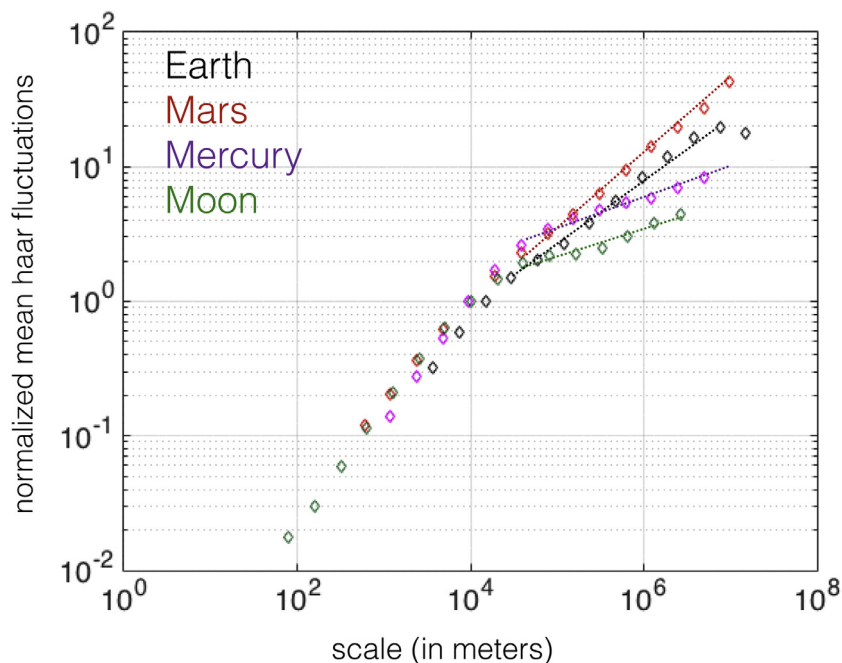


**Fig. 3.** Mean Haar fluctuations normalized in order to be approximately equal at scale 10 km, as a function of scale. The normalization does not modify the scaling behavior from Fig. 2 but emphasize the transition that seems to occur around 10 km.

fluctuations in topography rapidly increasing with the scale (structured aspect, high  $H$ ). The relief profile tends to be persistent since the slopes are highly correlated. At scales higher than  $T_e$ , a change in relief triggers an isostatic compensation which tends to oppose the large variations of the relief. The slopes of neighboring facets tend to be anti-correlated and the topographic profile is rougher. The topography oscillates around a mean value since the slopes are more anti-correlated. In this configuration, the altitude fluctuations increase only slightly regarding to scale (low  $H$ ). The common transition could be explained by the averaged value of the elastic thickness quite similar for the 5 bodies (Grott and Breuer, 2008; Barnett et al., 2000; Nimmo and Watters, 2004).

At scales larger than 10 km, all planetary bodies are different. Interestingly, the scaling law is characterized for the Moon by  $H = 0.2$ , Mercury by  $H = 0.3$ , Mars and Earth by  $H = 0.5$ . The smaller the body, the less intense its internal activity due to intense thermal cooling. The value of  $H$  may be related to its geological activity. One can speculate that a more intensively convecting mantle yields a higher value of  $H$ . This explanation links the large scale with dynamic topography (Hager et al., 1985). The fact that only large the scale topography is strongly multifractal is coherent with this explanation because multifractal behavior is related to fluid mechanics. The geological origin of this transition will be investigated in future works.

From our result, this pattern seems coherent other large ranges of

scale throughout the different bodies. Although suggesting that only a few processes might operate simultaneously at different scales, this result is not incompatible with the existence of processes operating at a specific altitude or locations. For example the “glacial buzz” saw effect seems limit the presence of high altitude on the Earth only (Lorenz et al., 2011). Our results simply suggest that the contribution of such process to global statistics can be neglected because if a strong altitude dependent process occurs, it should have broken the scaling behavior. It will be necessary to perform local analyses using the same methodology to fully understand the effect of altitude dependent and local processes on local statistic and how they correlate with multifractal parameters.

As a future work, we plan to perform local analysis on area defined by geological boundaries or altitude level to better understand the link between the scaling behavior of topography and natural processes operating at different location and altitude.

### Acknowledgments

We acknowledge support from the “Institut National des Sciences de l’Univers” (INSU), the “Centre National de la Recherche Scientifique” (CNRS) and “Centre National d’Etudes Spatiales” (CNES). This work was supported by the Programme National de Planétologie (PNP) and Programme National de Télédétection Spatiale (PNTS) of CNRS/INSU,

**Table 2**

Estimations of multifractal parameters. NA stands for non-applicable. If the value of  $C_1$  is very small (here  $< 0.02$ ), we can consider that the field is not multifractal and the value of  $\alpha$  is not meaningful.

Scale < 10 km	Earth	Mars	Moon	Mercury
$H$	$0.823 \pm 0.004$	$0.773 \pm 0.003$	$0.878 \pm 0.002$	$0.922 \pm 0.003$
$\alpha$	NA	NA	NA	NA
$C_1$	$0.01 \pm 0.01$	$0.02 \pm 0.006$	$0.02 \pm 0.04$	$0.026 \pm 0.005$
Scale > 10 km	Earth	Mars	Moon	Mercury
$H$	$0.479 \pm 0.001$	$0.53 \pm 0.001$	$0.226 \pm 0.002$	$0.248 \pm 0.002$
$\alpha$	$1.70 \pm 0.08$	$1.80 \pm 0.06$	$1.4 \pm 0.1$	$1.85 \pm 0.1$
$C_1$	$0.093 \pm 0.002$	$0.110 \pm 0.002$	$0.03 \pm 0.01$	$0.059 \pm 0.002$

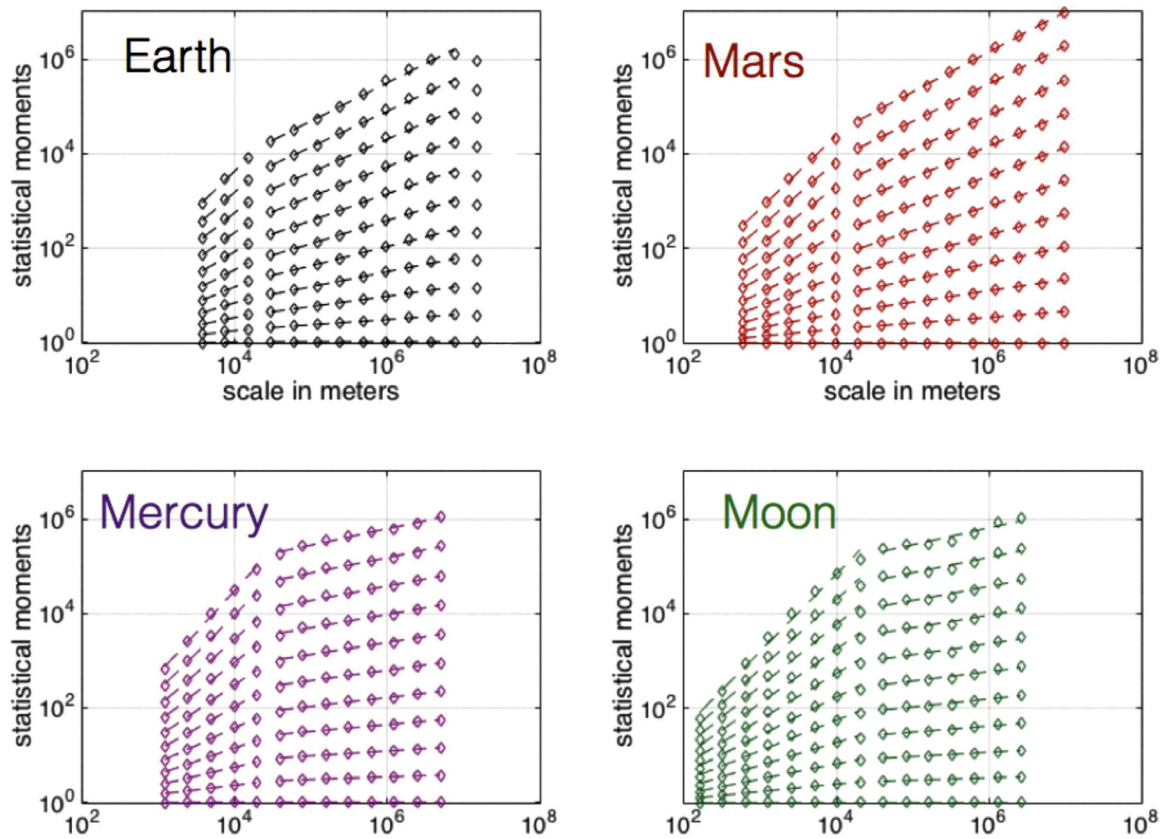


Fig. 4. Plot of different statistical moments for the four bodies. Although 21 moments have been computed for the purpose of this analysis (from 0.1 to 2 by steps of 0.1), only a few non-integers moments are plotted here for order 0.1 to order 2 by step of 0.2.

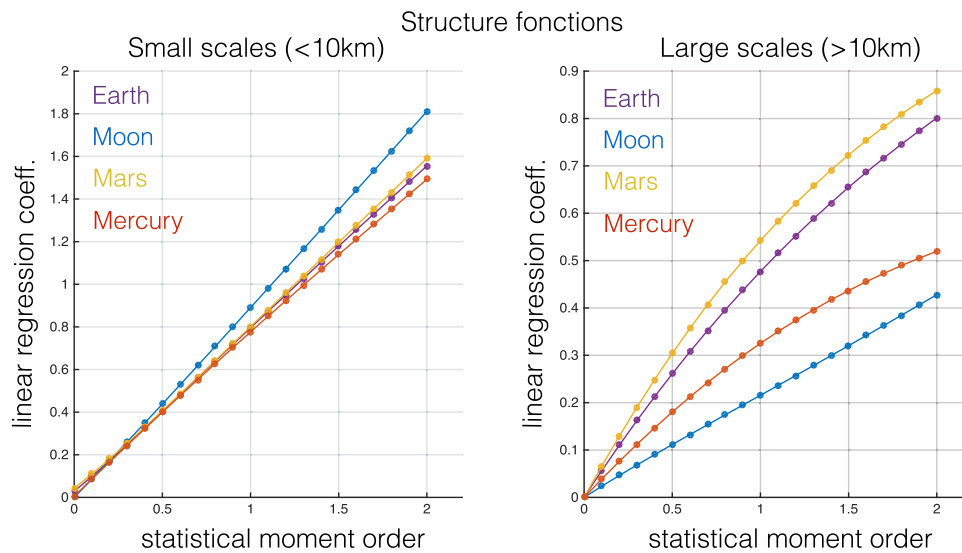


Fig. 5. Structure function for different ranges of scales.

co-funded by CNES.

### Appendix A. Annex: Bayesian regression

In order to estimate the best set of parameters ( $H, C_1, \alpha$ ) modeling the data, the parameters can be estimated in a classical way by performing regressions on the function  $\zeta$  near the mean ( $q = 1$ ) to quantify its curvature related to  $\alpha$  and  $C_1$  (Lovejoy and Shertzer, 2013) by the theoretical formulas:

$$H = \zeta(1)C_1 = \left. \frac{dK(q)}{dq} \right|_{q=1} \quad \alpha = \left. \frac{d^2K(q)}{dq^2} \right|_{q=1} / \left. \frac{dK(q)}{dq} \right|_{q=1} \quad (6)$$

As a reminder, the scaling exponents  $\zeta(q)$  are themselves the products of linear regression, so the fits from Eq. (6) are only indirectly related to the data. We wish to avoid this method which will not make possible to judge the quality of the estimates, especially as the multifractal component is rather weak when the function  $\zeta(q)$  is only weakly curved.

We propose a new approach based on principle of Bayesian inversion (Tarantola and Valette, 1982) which allows to construct a posterior probability distribution of the parameters (mean, most probable value, standard deviation) from observations. In practice, these distributions can be estimated iteratively by applying the Metropolis rule to construct a Monte Carlo Markov chain (Mosegaard and Tarantola, 1995) containing the different sets of parameters. We summarize the main lines of this technique, already used on photometry problems (Schmidt and Fernando, 2015; Fernando et al., 2013). As a first step, it is necessary to evaluate the quality of the individual linear regressions of each moment. In this step, we attribute to each point an empirical uncertainty with a centered gaussian distribution. The latter will be the higher as the linear correlation through the scale is accurate. Then, we tested the direct model, computed by applying the laws of Eqs. (4) and (5), for different random set of parameters ( $H, C_1, \alpha$ ). Synthetic realizations are then compared to observations. The Monte Carlo Markov chain is created according the metropolis rules, using the likelihood of empirical uncertainties. This method allow us to estimated realistic uncertainty bars on parameter ( $H, C_1, \alpha$ ), from the observational data (see Table 2).

## Supplementary material

Supplementary material associated with this article can be found, in the online version, at doi:10.1016/j.icarus.2018.07.005.

## References

- Aharonson, O., Zuber, M.T., Rothman, D.H., 2001. Statistics of Mars' topography from the mars orbiter laser altimeter: Slopes, correlations, and physical models. *J. Geophys. Res.: Planets* 106 (E10), 23723–23735. <https://doi.org/10.1029/2000JE001403>.
- Amante, C., Eakins, B., 2009. Etopo1 1 arc-minute global relief model: procedures, data sources and analysis. NOAA Technical Memorandum NESDIS NGDC-24. National Geophysical Data Center, NOAA.
- Araki, H., et al., 2009. Lunar global shape and polar topography derived from Kaguya-lalt laser altimetry. *Science* 323 (5916), 897–900.
- Barnett, D.N., Nimmo, F., McKenzie, D., 2000. Elastic thickness estimates for Venus using line of sight accelerations from Magellan cycle 5. *Icarus* 146 (2), 404–419.
- Bills, B.G., Asmar, S.W., Konopliv, A.S., Park, R.S., Raymond, C.A., 2014. Harmonic and statistical analyses of the gravity and topography of Vesta. *Icarus* 240, 161–173.
- Bondarenko, N., Kreslavsky, M., Head, J., 2006. North-south roughness anisotropy on Venus from the Magellan radar altimeter: correlation with geology. *J. Geophys. Res.: Planets* 111 (E6).
- Cavanaugh, J.F., et al., 2007. The Mercury Laser Altimeter Instrument for the MESSENGER Mission. Springer New York, New York, NY, pp. 451–479.
- Deliege, A., Kleynssens, T., Nicolay, S., 2016. The Fractal Nature of Mars Topography Analyzed via the Wavelet Leaders Method. Springer International Publishing, Cham, pp. 1295–1298.
- Dodds, P.S., Rothman, D.H., 2000. Scaling, universality, and geomorphology. *Annu. Rev. Earth Planet. Sci.* 28 (1), 571–610. <https://doi.org/10.1146/annurev.earth.28.1.571>.
- Fernando, J., Schmidt, F., Ceamanos, X., Pinet, P., Douté, S., Daydou, Y., 2013. Surface CO<sub>2</sub> reflectance of CO<sub>2</sub> Mars observed by CRISM/MRO: 2. Estimation of surface photometric properties in Gusev crater and Meridiani Planum. *J. Geophys. Res.: Planets* 118, 534–559. <https://doi.org/10.1029/2012JE004194>.
- Ford, P., Pettengill, F., Liu, G., J., Q., 2014. Magellan global topography 4641m. PDS GeoScience Node.
- Gagnon, J.-S., Lovejoy, S., Schertzer, D., 2006. Multifractal earth topography. *Nonlinear Process Geophys.* 13 (5), 541–570. <https://doi.org/10.5194/npg-13-541-2006>.
- Grott, M., Breuer, D., 2008. The evolution of the martian elastic lithosphere and implications for crustal and mantle rheology. *Icarus* 193 (2), 503–515.
- Hager, B.H., Clayton, R.W., Richards, M.A., Comer, R.P., Dziewonski, A.M., 1985. Lower mantle heterogeneity, dynamic topography and the geoid. *Nature* 313 (6003), 541–545.
- Hawkins, S.E., et al., 2007. The Mercury dual imaging system on the messenger spacecraft. *Space Sci. Rev.* 131 (1), 247–338.
- Kreslavsky, M., Head, J., 2003. North-south topographic slope asymmetry on Mars: evidence for insolation-related erosion at high obliquity. *Geophys Res Lett* 30 (15).
- Kreslavsky, M.A., Head, J.W., 2000. Kilometer-scale roughness of Mars: results from MOLA data analysis. *J. Geophys. Res.: Planets* 105 (E11), 26695–26711. <https://doi.org/10.1029/2000JE001259>.
- Kreslavsky, M.A., Head, J.W., Neumann, G.A., Rosenburg, M.A., Aharonson, O., Smith, D.E., Zuber, M.T., 2013. Lunar topographic roughness maps from lunar orbiter laser altimeter (LOLA) data: scale dependence and correlation with geologic features and units. *Icarus* 226 (1), 52–66. <https://doi.org/10.1016/j.icarus.2013.04.027>.
- Landais, F., Schmidt, F., Lovejoy, S., 2015. Universal multifractal martian topography. *Nonlinear Process Geophys.* 22 (6), 713–722. <https://doi.org/10.5194/npg-22-713-2015>.
- Lavallee, D., Lovejoy, S., Schertzer, D., Ladoy, P., 1993. Nonlinear variability and landscape topography: analysis and simulation. In: De Cola, L., Lam, N. (Eds.), *Fractals in Geography*. PTR, Prentice Hall, pp. 158–192.
- Lorenz, R.D., Turtle, E.P., Stiles, B., Gall, A.L., Hayes, A., Aharonson, O., Wood, C.A., Stofan, E., Kirk, R., 2011. Hypsometry of Titan. *Icarus* 211 (1), 699–706.
- Lovejoy, S., 2014. A voyage through scales, a missing quadrillion and why the climate is not what you expect. *Clim. Dyn.*
- Lovejoy, S., Schertzer, D., 2013. *The Weather and Climate: Emergent Laws and Multifractal Cascades*. Cambridge University Press, Cambridge.
- Malamud, B.D., Turcotte, D.L., 2001. Wavelet analyses of Mars polar topography. *J. Geophys. Res.: Planets* 106 (E8), 17497–17504. <https://doi.org/10.1029/2000JE001333>.
- Mandelbrot, B., 1967. How long is the coast of Britain? statistical self-similarity and fractional dimension. *Science* 156 (3775), 636–638. <https://doi.org/10.1126/science.156.3775.636>.
- Mosegaard, K., Tarantola, A., 1995. Monte Carlo sampling of solutions to inverse problems. *J. Geophys. Res.: Solid Earth* 100 (B7), 12431–12447.
- Nimmo, F., Bills, B., Thomas, P., 2011. Geophysical implications of the long-wavelength topography of the saturnian satellites. *J. Geophys. Res.: Planets* 116 (E11).
- Nimmo, F., Watters, T., 2004. Depth of faulting on Mercury: implications for heat flux and crustal and effective elastic thickness. *Geophys Res. Lett.* 31 (2).
- Orosei, R., Bianchi, R., Coradini, A., Espinasse, S., Federico, C., Ferriccioni, A., Gavrishin, A.I., 2003. Self-affine behavior of martian topography at kilometer scale from Mars orbiter laser altimeter data. *J. Geophys. Res.: Planets* 108 (E4), n/a–n/a, doi:10.1029/2002JE001883.
- Pommerol, A., Chakraborty, S., Thomas, N., 2012. Comparative study of the surface roughness of the Moon, Mars and Mercury. *Planet. Space Sci.* 73, 287–293.
- Richardson, L.F., 1961. The problem of contiguity: an appendix to statistic of deadly quarrels. *Gen. Syst.* 61, 139–187.
- Rosenburg, M.A., Aharonson, O., Head, J.W., Kreslavsky, M.A., Mazarico, E., Neumann, G.A., Smith, D.E., Torrence, M.H., Zuber, M.T., 2011. Global surface slopes and roughness of the moon from the lunar orbiter laser altimeter. *J. Geophys. Res.: Planets* 116 (E2), n/a–n/a. <https://doi.org/10.1029/2010JE003716>.
- Schertzer, D., Lovejoy, S., 1987. Physical modeling and analysis of rain and clouds by anisotropic scaling multiplicative processes. *J. Geophys. Res.: Atmospheres* 92 (D8), 9693–9714. <https://doi.org/10.1029/JD092iD08p09693>.
- Schmidt, F., Fernando, J., 2015. Realistic uncertainties on hApke model parameters from photometric measurement. *Icarus* 260, 73–93.
- Smith, D.E., et al., 2001. Mars orbiter laser altimeter: experiment summary after the first year of global mapping of Mars. *J. Geophys. Res.: Planets* 106 (E10), 23689–23722. <https://doi.org/10.1029/2000JE001364>.
- Smith, D.E., et al., 2010. The lunar orbiter laser altimeter investigation on the lunar reconnaissance orbiter mission. *Space Sci. Rev.* 150 (1), 209–241. <https://doi.org/10.1007/s11214-009-9512-y>.
- Solomon, S.C., et al., 2001. The messenger mission to Mercury: scientific objectives and implementation. *Planet. Space Sci.* 49 (14), 1445–1465.
- Stiles, B.W., et al., 2009. Determining Titan surface topography from Cassini (SAR) data. *Icarus* 202 (2), 584–598. <https://doi.org/10.1016/j.icarus.2009.03.032>.
- Tarantola, A., Valette, B., 1982. Generalized nonlinear inverse problems solved using the least squares criterion. *Rev. Geophys.* 20 (2), 219–232.